PERGAMON

International Journal of Solids and Structures 38 (2001) 3979–3994

INTERNATIONAL JOURNAL OF SOLIDS and STRUCTURES

www.elsevier.com/locate/ijsolstr

Thermal buckling of rectangular plates

Kevin D. Murphy *, David Ferreira

Department of Mechanical Engineering, University of Connecticut, 191 Auditorium Road, U-139, Storrs, CT 06269-3139, USA

Received 8 September 1999; in revised form 26 May 2000

Abstract

This paper presents the results of a thermal buckling analysis for clamped, rectangular plates based on energy considerations. The analysis reveals that both of the edge length to thickness ratios $(a/h, b/h)$ are independent parameters, i.e. fixing the aspect ratio (a/b) is not sufficient to ensure a unique problem. The results also show that predictable modal groupings and curve veering occur in the eigenvalue loci as the aspect ratio is varied. Accompanying this analysis are a series of experiments to determine the buckling temperature for plates with varying edge length. However, measurements of the critical temperature for flat plates, $T_{\mathrm{cr}}^{\mathrm{F}}$, are complicated by the fact that initial geometric imperfections are inherent in any real structure. In this case, the pitchfork bifurcation associated with buckling is replaced by a saddle-node bifurcation at $T_{\mathrm{cr}}^{\mathrm{Im}}$, which is easily measured. An analysis is performed using von Kármán plate theory to determine the ratio of $T_{\mathrm{cr}}^{\mathrm{F}}/T_{\mathrm{cr}}^{\mathrm{Im}}$ as a function of the initial imperfection size $\tilde{A}$. Knowing this functional relationship and the measured values of $\tilde{A}$ and $T_{\mathrm{cr}}^{\mathrm{Im}}$, the flat plate buckling temperature may be determined. Comparisons between the buckling analysis and the experimental results show good agreement. © 2001 Elsevier Science Ltd. All rights reserved.

Keywords: Thermal buckling; Experiments

1. Introduction

Buckling studies for thin structures are deeply rooting in the history of mechanics. The first and, arguably, most famous work was carried out by Euler in 1744 and resulted in the buckling load for a pinned–pinned beam. However, buckling is *not* simply an interesting yet irrelevant subject which was solved and left in the eighteenth century. The lateral stability of beams, plates, shells, etc. continue to be a relevant engineering problem in the design of aircraft and seacraft as weight requirements drive designers to thinner structures which are more susceptible to static instabilities. Furthermore, the development of new materials with new constitutive models have necessitated continued research in stability.

In the literature, a wide variety of geometries, boundary conditions, and constitutive models have been considered. Because of the depth and breadth of the subject, a complete survey of the work since Euler's initial efforts would be almost impossible to amass. However, a summary of many recent developments in

---

* Corresponding author. Fax: +1-860-486-5088.
E-mail address: kdm@engr.uconn.edu (K.D. Murphy).

PII: S0020-7683(00)00240-7

this field are presented in the two IUTAM volumes by Budiansky (1976) and Thompson and Hunt (1983) and, for the case of thermal buckling, in the review articles by Tauchert (1991) and Thornton (1993).

The present work takes a combined theoretical and experimental approach to determine the buckling temperature and buckling mode for a flat, rectangular plate which is fully clamped (both in plane and out of plane). The theoretical effort involves a linear energy analysis leading to a buckling eigenvalue problem. The experimental effort, which constitutes the principle focus of this work, involves a newly developed technique for determining the buckling load. Such measurements are useful since (i) they provide fundamental insight into the character of the structure, (ii) they set a safe upper bound for the loading – since buckling is usually undesirable and (iii) people often choose to nondimensionalize temperature by the linear buckling temperature, i.e. they specify the temperature as a percent of the buckling temperature. Hence, accurate measurements of the buckling temperature are required for consistent comparisons with theoretical results.

There are many ways to estimate experimentally the buckling load as described by Souza et al. (1983). However, the three most typical approaches are briefly described here. In the first method, the buckling load is estimated, often by eye, from the axial load vs. displacement curve (Hoff et al., 1948). The shortcomings of this approach are self-evident. Alternately, Southwell (1932) developed a technique to measure the buckling load using deformation–load data and the linear asymptotic behavior of the deformation as buckling is approached. These estimates usually have to be made with very few data points and are not always reliable. The third approach uses frequency information to estimate the buckling load (Plaut and Virgin, 1990; Murphy et al., 1997). Though more reliable than the other approaches, this method is largely restricted to the low compressive load range – limiting the amount of data used in the estimate.

To circumvent these problems, a new and reliable method for consistently determining the buckling temperature is presented here. This new method also uses the load–displacement behavior but incorporates nonlinear effects and only requires the measurement of two quantities. To explain this, consider Fig. 1. This schematic shows the equilibrium deflection of two plates: one is perfectly flat, and the other possessing an initial imperfection. The perfectly flat plate undergoes a symmetric pitchfork bifurcation at the buckling temperature, $T^{\mathrm{F}}_{\mathrm{cr}}$. In contrast, the imperfect plate develops an unsymmetric secondary state by means of a saddle-node bifurcation at a higher temperature, $T^{\mathrm{Im}}_{\mathrm{cr}}$. The key to obtaining the flat plate buckling load is to recognize that the separation between the two bifurcations is a function of the imperfection size (large imperfections lead to a greater separation). Von Kármán plate theory is then used to develop a functional relationship between the critical temperature ratio and the size of the initial imperfection: $T^{\mathrm{F}}_{\mathrm{cr}}/T^{\mathrm{Im}}_{\mathrm{cr}} = f(\tilde{A})$.

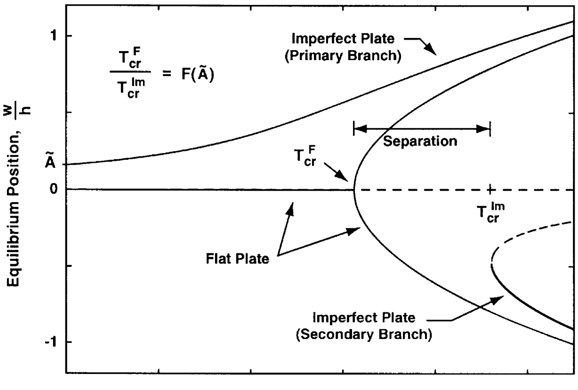

Fig. 1. A schematic equilibrium position vs. temperature diagram for a perfectly flat plate and an initially imperfect (curved) plate.

Hence, by measuring the initial imperfection size ($\tilde{A}$) and the critical load for the imperfect plate ($T_{\mathrm{cr}}^{\mathrm{Im}}$), both of which are easily obtained, the flat plate buckling temperature may be determined.

2. Buckling analysis

In this section, a model is developed to predict the temperature at which the flat equilibrium configuration of a rectangular plate loses stability. The analytical approach presented here requires that the in-plane boundary conditions are fully fixed (no in-plane displacements at the edges) while a variety of out-of-plane conditions may be considered. For the sake of the experiments, the results of this model will focus on plates with fully clamped out-of-plane boundary conditions on all four sides.

Because initial buckling corresponds to an unbounded solution in the linearized system, a linear analysis is sufficient to obtain the thermal buckling characteristics of the plate. In dimensional form, the linearized strain energy per unit thickness, U, for the flat plate takes the form

$$U = \int_0^a \int_0^b \left[N_x\epsilon_{xs} + N_y\epsilon_{ys} + N_{xy}\epsilon_{xys}\right] \mathrm{d}x\,\mathrm{d}y + \frac{D}{2}\int_0^a \int_0^b \left[W_{,xx}^2 + W_{,yy}^2 + 2vW_{,xx}W_{,yy} + 2(1-v)W_{,xy}^2\right] \mathrm{d}x\,\mathrm{d}y, \tag{1}$$

where W is the out-of-plane displacement field, D is the plate bending stiffness, N_x and N_y are the in-plane loads, ϵ_{xs}, ϵ_{ys}, ϵ_{xys} are the stretching components of the strains, and v is Poisson's ratio. Note that the comma notation refers to differentiation ($\bullet_{,\xi} \equiv \mathrm{d}\bullet/\mathrm{d}\xi$). The first term represents the energy due to in-plane stretching while the second term corresponds to the bending energy. Also, the compressive in-plane biaxial loads are assumed to be proportional to the temperature rise (Boley and Weiner, 1965). In other words, $N_x = N_y = -(Eh/(1-v))\alpha T$ and $N_{xy} = 0$. Here, E is the elastic modulus, h, the plate thickness, α, the thermal expansion coefficient, and T, the temperature rise above ambient temperature. Substituting these expressions into Eq. (1) gives the strain energy in terms of the out-of-plane displacement field. Appropriately nondimensionalized, the strain energy may be written as

$$U = -\alpha T F_1(w) + F_2(w), \tag{2}$$

where

$$F_1 = 12(1+v)\left(\frac{b}{h}\right)^2 \int_0^1 \int_0^1 \left(w_{,\xi}^2 + \phi^2 w_{,\eta}^2\right) \mathrm{d}\xi\,\mathrm{d}\eta, \tag{3}$$

$$F_2 = \int_0^1 \int_0^1 \left[\frac{1}{\phi^2} w_{,\xi\xi}^2 + \phi^2 w_{,\eta\eta}^2 + 2v w_{,\xi\xi} w_{,\eta\eta} + 2(1-v) w_{,\xi\eta}^2\right] \mathrm{d}\xi\,\mathrm{d}\eta. \tag{4}$$

Also, the nondimensional lateral displacement is $w = W/h$, the spatial coordinates are $\xi = x/a$, $\eta = y/b$, and $\phi = a/b$ is the aspect ratio. Using a set of functions $\Psi_i(\xi,\eta)$ which satisfies the geometric boundary conditions, the displacement is written as an expansion: $w(\xi,\eta) = \sum a_i \Psi_i(\xi,\eta)$. In particular, the functions Ψ_i used in this study are a product of the clamped–clamped beam vibration mode shapes in the ξ and η directions. The equilibrium configurations are then found by evaluating $\partial U/\partial a_i = 0$. This results in a general eigenvalue problem of the form

$$\left[\frac{\partial F_2}{\partial a_i}\right]\{a_i\} = \alpha T \left[\frac{\partial F_1}{\partial a_i}\right]\{a_i\}. \tag{5}$$

The matrices are coupled, and their elements result from the spatial integration of the expansion functions in Eqs. (3) and (4). The eigenvalues for this problem are the critical temperatures, the smallest of which constitutes the thermal buckling load, $T_{\mathrm{cr}}^{\mathrm{F}}$. The buckling mode can be deduced by examining the associated eigenvector.

It should be noted that, in Eq. (3), the x and y length scales cannot be written solely in terms of the aspect ratio ϕ (note the b in the coefficient of F_1). This suggests that a and b are independent parameters. Throughout this work, a/h and b/h are viewed as the two relevant parameters and $\phi = (a/h)(h/b)$ is an alternative, but dependent, parameter.

3. Experiments

3.1. Experimental setup

Fig. 2 shows a schematic of the experimental setup. A 0.3175 mm (0.125 in.) thick aluminum plate (A) was securely sandwiched between two sides of a test frame (B), as indicated by the inset. A total of 28, 12.7 mm (0.5 in.) bolts were evenly spaced around the edge of the frame to maintain the zero displacement boundary conditions (both in plane and out of plane). The frame was constructed from a high chromium steel, chosen for its low coefficient of thermal expansion. This prevents appreciable expansion of the frame during high temperature tests. To further limit the expansion of the frame, a flushing channel was machined into the inside perimeter of the frame, where heat transfer from the plate to the frame is largest; again, see the inset. Using a chiller, a water/glycol mixture was continuously circulated through coolant lines to the flushing channel at a rate of 41.6 l/min. The chiller was able to keep the frame at ambient even while test plates were heated to approximately 100°C. The steel frame was built with an adjustable side (C) to accommodate plates with different aspect ratios. Smaller plates were secured in place by sliding the adjustable side (C) along the y-axis to the proper width dimension. Cooling fluid was also supplied to the adjustable side (C) using PVC tubing.

Heat was applied to the plate using six 1300 W, three phase heating elements (D). The heating elements, located 12.7 cm from the plate surface, were evenly spaced to promote an even temperature distribution. The plate surface was treated with a high temperature flat-black paint to promote heat absorption of the normally reflective aluminum surface. The heaters were computer controlled using LabVIEW software. A thermocouple, mounted to the center of both sides of the plate provided the reference for the temperature control. Omega-Bond was used to attach the thermocouple to the plate; this provided good adhesion and

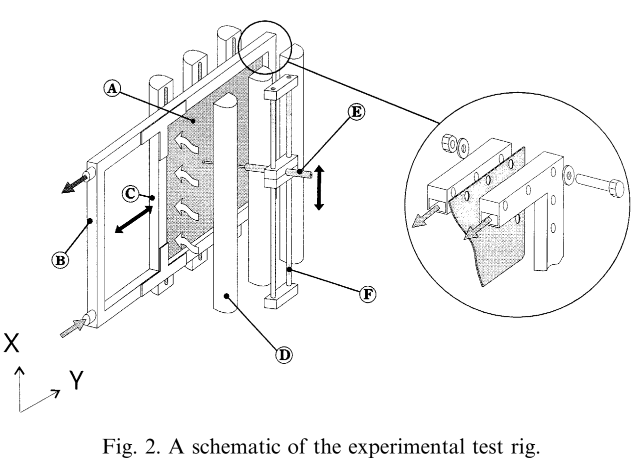

Fig. 2. A schematic of the experimental test rig.

isolated the thermocouple from external conditions. Each side of the plate utilized its own independent control loop allowing the plate temperature to be carefully monitored and maintained.

Preliminary tests were performed to ensure that a uniform temperature distribution resulted. This entailed outfitting a test plate with 16 evenly spaced thermocouples and recording the temperatures at various set points. At the edges of the plate, where the plate contacted the frame, the plate tended to be cooler due to conduction; the edge temperature was typically 90% of the center temperature. Attempts to limit this temperature variation at the edges focused on placing various insulative material between the plate and the frame. However, these materials allowed in-plane slipping of the plate (on the order of 0.0245 mm) due to (i) the flexibility in the insulation and (ii) the high resultant in-plane forces in the plate due to the elevated temperatures. This mild slipping dramatically changed the buckling results, i.e. increased the buckling temperature. Therefore, a decision was made to remove the insulation and ignore the small temperature variation over the plate.

The initial imperfection of the plate and any deformations due to temperature changes were measured with a linear voltage displacement transducer, or LVDT (E), mounted to a vertical slide (F). The voltage signal from the LVDT was sent to the computer and converted to a displacement reading using an appropriate calibration. Moving the LVDT vertically along the length of the plate and recording the corresponding displacement readings generated a deflection profile for the plate.

3.2. Experimental procedure

The aim of these experiments was to determine the buckling temperatures and mode shapes of a fully clamped rectangular plate of various dimensions. This was accomplished by developing an equilibrium displacement vs. temperature diagram for each plate (each with a different aspect ratio), similar to that shown in Fig. 1, and recording T_{cr}^{Im}. Knowing T_{cr}^{Im} and the imperfection size $\tilde{A}$, one can easily obtain T_{cr}^{F} using the method outlined in Section 3.3. The remainder of this section explains the procedure for generating the equilibrium displacement vs. temperature diagram and the initial imperfection profile for a single plate.

To begin, the plate was mounted in the test frame and the adjustable side was fitted to that plate's particular dimensions. With the plate in place, the frame halves were clamped together using a series of 1.27 cm (1/2 in.) coarse-thread bolts. The bolts were installed into pre-drilled 1.35 cm (17/32 in.) bolt holes with a separation of 10.16 cm (4 in.) between bolt holes. The holes were slightly oversized to ensure that the bolts themselves would not induce any unwanted forces on the plate. To ensure proper seating of the plate in the frame, the bolts were tightened in an alternating pattern. The clamping sequence involved initially tightening all the bolts to 27.12 Nm (20 ft lb) and incrementally increasing the torque until a final torque of 122 Nm (90 ft lb) was achieved. This torque value translates into a clamping force of approximately 44.5 kN (10,000 lb) per bolt.

It would be ideal to run these experiments on perfectly flat aluminum plates but the manufacturing process, handling and machining of the plates have induced small imperfections in the test pieces. The initial deformations were measured with the LVDT. The LVDT was mounted on a slide that traveled on two vertical rails (Fig. 2). The LVDT and rails were calibrated to ensure that the displacement measurements reflected *only* the plate's deflection and not the slight curvature that may be present in the LVDT rails. The initial plate imperfection was recorded by running the LVDT along a vertical length of the plate and recording data points at 2.54 cm (1 in.) intervals. A plate profile was generated using the acquired data and the aforementioned calibration. This profile was analyzed for its modal content (using the buckling modes for a fully clamped plate as the basis functions) using a least-squares fit. The information from the least-squares fit was used to determine which mode was dominant in the initial imperfection and how that shape could affect the buckling phenomenon.

With the plate securely mounted and the chiller maintaining the frame at room temperature, heat was applied to both sides of the plate. The temperature was incremented in small steps using the data acquisition and control software. Each side of the plate was heated to the setpoint using a central thermocouple (one on each side) for feedback. The heaters could not vary the amount of heat they produced, so the heat banks were cycled on and off to achieve the setpoint temperatures. A digital on-off controller or "bang–bang" controller with hysteresis about the setpoint was used as a thermostat to maintain the desired temperatures. The center of the plate was maintained at the desired level but a small temperature gradient was present across the surface of the plate. The cool frame as well as the natural convection from the surrounding areas helped to create these mild temperature variations (as much as 10%) across the plate.

To determine experimentally the buckling temperature, the heaters were cycled on to gradually increase the plate's temperature. The plate was periodically checked for signs of multiple equilibria throughout the heating process. The existence (or nonexistence) of multiple equilibria was determined by pushing on the plate in the direction opposite to the initial imperfection and observing the plate's reaction. If the plate popped back to its original position when released, the secondary equilibrium state was not yet stable. If the plate stayed in its new configuration, that state was deemed stable.

Once the plate was stable in its secondary equilibrium position, the plate temperature was increased by a few degrees and a slow cooling process was started. During the cooling process, the out-of-plane displacements were recorded with the LVDT. Placement of the LVDT was critical since nodal lines had to be avoided. Because the third mode was the highest expected to participate (for the plate dimensions considered here), the LVDT was placed midway between the nodal lines for the second and third modes. As the plate cooled, displacement and temperature readings were taken at regular intervals. As the plate traversed $T_{\mathrm{cr}}^{\mathrm{Im}}$, it "popped back" into its primary equilibrium configuration and then returned to its original shape as the plate reached room temperature. To get the entire primary branch, the plate was heated again past the buckling temperature and allowed to cool without pushing it through to its secondary equilibrium state. LVDT and temperature data were again recorded.

Finally, once the equilibrium position vs. temperature diagram is mapped, the buckling mode must be ascertained. This was accomplished by re-heating the plate to a temperature just above $T_{\mathrm{cr}}^{\mathrm{Im}}$ and using the LVDT to measure a profile of the plate at discrete points. The profile clearly indicated which was the buckling mode. Since only the first mode was expected in the y-direction (the axis being shrunk, see Fig. 2), the location of the LVDT on the horizontal axis was chosen as close to the center of the plate as possible without interfering with the heaters.

3.3. A method for determining T_{cr}^{F}

The difficulty in measuring the flat plate buckling temperature is that all real plates have some initial geometric imperfection. This initial curvature produces a change in the bifurcation phenomenon experienced by the plate. As shown qualitatively in Fig. 1, the pitchfork bifurcation is replaced by a saddle-node bifurcation. As a result, the location of the buckling temperature $T_{\mathrm{cr}}^{\mathrm{F}}$ is not easily identified by looking at the displacement–temperature curve from actual data (the imperfect case). To remedy this matter, one observation is critical: the separation between $T_{\mathrm{cr}}^{\mathrm{F}}$ and $T_{\mathrm{cr}}^{\mathrm{Im}}$ is a function of the size of the initial imperfection, i.e. more curvature leads to a greater separation. The remainder of this section is devoted to developing analytical expressions relating $T_{\mathrm{cr}}^{\mathrm{F}}$ and $T_{\mathrm{cr}}^{\mathrm{Im}}$ in terms of the imperfection size. The pitchfork bifurcation temperature is then written as a percent of the saddle-node temperature. In other words, they are expressed in functional form as

$$\frac{T_{\mathrm{cr}}^{\mathrm{F}}}{T_{\mathrm{cr}}^{\mathrm{Im}}} = f(\tilde{A}). \tag{6}$$

Knowing this functional relation and measuring $T_{\mathrm{cr}}^{\mathrm{Im}}$ and $\tilde{A}$, one can easily obtain $T_{\mathrm{cr}}^{\mathrm{F}}$.

To begin, consider the algebraic form of the equilibrium equation for a single mode representation of a rectangular plate subjected to a uniform temperature field

$$(\gamma_1)A^3 + (\gamma_2\tilde{A})A^2 + (\gamma_3\tilde{A}^2 + \gamma_4 + \gamma_5\alpha T)A + (\gamma_6\tilde{A}\alpha T) = 0, \tag{7}$$

where A is the nondimensional modal displacement, $\tilde{A}$, the nondimensional modal amplitude of the imperfection, the γ_i's are Galerkin coefficients, T, the temperature rise above ambient, and α, the coefficient of thermal expansion. This equation was obtained from von Kármán plate theory and Galerkin's method as described in Appendix A. Two things should be noted regarding this equation and the following analysis. First, the form of Eq. (7) is independent of the out-of-plane boundary conditions. Different boundary conditions would only change the assumed displacement function $\Psi_{ij}(\xi,\eta)$ and, hence, the Galerkin coefficients. Second, it is assumed that there is no in-plane motion at the boundaries, i.e. it is fully fixed in plane.

For the perfectly flat plate, the equilibrium equation reduces to $A(\gamma_1 A^2 + \gamma_4 + \gamma_5\alpha T) = 0$. The roots are $A = 0$ and $A = \pm\sqrt{(-\gamma_4 - \gamma_5\alpha T)/\gamma_1}$. As shown in Fig. 1, the occurrence of the pitchfork bifurcation corresponds to three real, coincident roots. Specifically, the roots must all be zero. Therefore, $(-\gamma_4 - \gamma_5\alpha T)/\gamma_1 = 0$ and the buckling load becomes

$$T_{\text{cr}}^{\text{F}} = \frac{-1}{\alpha}\left(\frac{\gamma_4}{\gamma_5}\right). \tag{8}$$

Determining $T_{\text{cr}}^{\text{Im}}$ is conceptually no different than the flat plate case but is more algebraically tedious. To begin, the following definitions are made $\epsilon_1 = \gamma_2\tilde{A}/\gamma_1$, $\epsilon_2 = (\gamma_2\tilde{A}^2 + \gamma_4 + \gamma_5\alpha T)/\gamma_1$, and $\epsilon_3 = \gamma_6\tilde{A}\alpha T/\gamma_1$. Using these expressions, the equilibrium equation becomes

$$A^3 + \epsilon_1 A^2 + \epsilon_2 A + \epsilon_3 = 0. \tag{9}$$

Making the further substitution $A = A_0 - \epsilon_1/3$ puts the equilibrium equation in the standard form:

$$A_0^3 = \left[\tfrac{1}{3}\epsilon_1^2 - \epsilon_2\right]A_0 + \left[-\tfrac{2}{27}\epsilon_1^3 + \tfrac{1}{3}\epsilon_1\epsilon_2 - \epsilon_3\right]. \tag{10}$$

Exact solutions for A_0 are well known (Meriam and Kraige, 1992). Assuming that $p_1 = \frac{1}{3}(\frac{1}{3}\epsilon_1^2 - \epsilon_2)$ and $q_1 = \frac{1}{2}(-\frac{2}{27}\epsilon_1^3 + \frac{1}{3}\epsilon_1\epsilon_2 - \epsilon_3)$, three solution classes appear: (i) $q_1^2 - p_1^3 < 0$ and there are three real, distinct roots, (ii) $q_1^2 - p_1^3 = 0$ and there are three real roots, two of which are repeated, and (iii) $q_1^2 - p_1^3 > 0$ and there is one real and two imaginary roots. By comparing the number of real roots with Fig. 1, it is evident that these cases correspond to being above, at, and below $T_{\text{cr}}^{\text{Im}}$ (the saddle-node point), respectively. Therefore, $T_{\text{cr}}^{\text{Im}}$ may be obtained by solving the equation $q_1^2 - p_1^3 = 0$.

Substituting the expressions for p_1, q_1, and the ϵ_i's into $q_1^2 - p_1^3 = 0$, yields a cubic equation in T:

$$T^3 + C_2T^2 + C_1T + C_0 = 0, \tag{11}$$

where the coefficients C_i are given in Appendix B. The solution to this equation *is* $T_{\text{cr}}^{\text{Im}}$. This may be solved by expressing it in standard form. Let $T = T_0 - C_2/3$. This leads to

$$T_0^3 = \left[-C_1 + \frac{C_2^2}{3}\right]T_0 + \left[-C_0 + \frac{C_1C_2}{C_3} - \frac{2C_2^3}{27}\right]. \tag{12}$$

Assuming that $p_2 = \frac{1}{3}\left(-C_1 + (C_2^2/3)\right)$ and $q_2 = \frac{1}{2}\left(-C_0 + (C_1C_2/C_3) - (2C_2^3/27)\right)$, it may be shown that there is only one real root to this equation (the other two roots are complex). This root is

$$T_0 = \left(q_2 + \sqrt{q_2^2 - p_2^3}\right)^{1/3} + \left(q_2 - \sqrt{q_2^2 - p_2^3}\right)^{1/3}. \tag{13}$$

Therefore, the critical temperature for the imperfect plate is simply

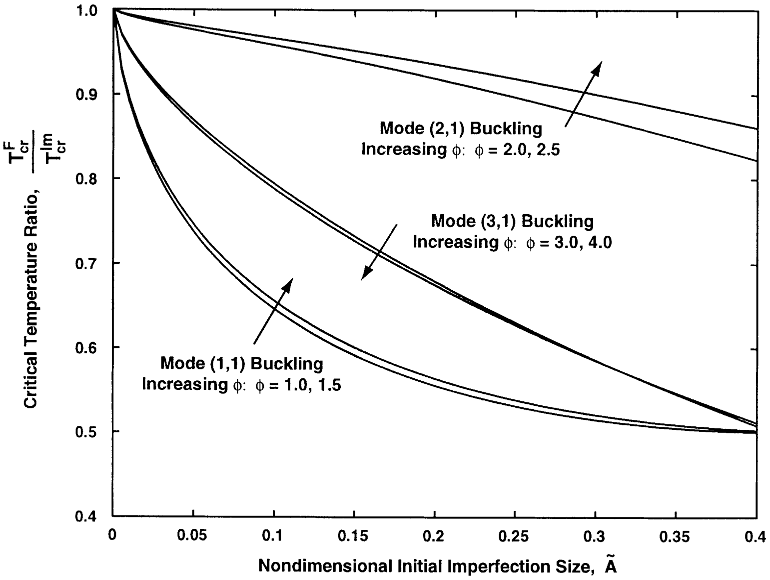

Fig. 3. The critical temperature ratio T_{cr}^{F}/T_{cr}^{Im} as a function of the imperfection size for plates of various aspect ratio.

$$T_{cr}^{Im} = \left(q_2+\sqrt{q_2^2-p_2^3}\right)^{1/3} + \left(q_2-\sqrt{q_2^2-p_2^3}\right)^{1/3} - \frac{C_2}{3}. \tag{14}$$

The separation between the critical temperatures (Fig. 1) may be expressed as the ratio of T_{cr}^{F} to T_{cr}^{Im} as computed using Eqs. (8) and (14). Fig. 3 shows the behavior of the critical temperature ratio as a function of the initial imperfection size. In this case, the edge length to thickness ratio is kept constant at $a/h = 240$ while various $b/h(= a/h \times 1/\phi)$ values are considered. Here, the initial imperfection is assumed to be in the (1,1) mode shape. Three groups of curves appear for aspect ratios in the range of $1.0 \leqslant \phi \leqslant 4.0$; each group relates to a different buckling mode. Several observations should be made. First, for all imperfection sizes and all aspect ratios, the critical temperature ratio is less than or equal to one. This makes physical sense as the presence of an imperfection stiffens the system delaying the bifurcation as shown schematically in Fig. 1. Second, as the initial imperfection vanishes, the critical temperature ratio approaches one for all cases. In other words, as the imperfection gets smaller, the plate begins to act more and more like a flat plate. Finally, for the case of first mode buckling, as the imperfection gets large (say, $\tilde{A} > 0.35$, meaning that the maximum initial deflection exceeds $0.35h$), the critical temperature ratio flattens out, i.e. T_{cr}^{F} approaches a fixed percentage of T_{cr}^{Im}. This is not consistent with experimental observations. This breakdown of the theory can be explained by the fact that only *small* imperfections are taken into account (Appendix A). A large imperfection theory could be developed but would significantly increasing the complexity of the solution procedure. Fortunately, small imperfections ($\tilde{A} < 0.35$) are the norm.

4. Results

Five different plates were used in the tests. All were made of stock aluminum, had a thickness of $h = 3.175$ mm (0.125 in.), and had one fixed dimension of $a = 76.2$ cm (30 in.). The other edge length was varied and had values of $b/h = 192, 160, 120, 106.6, 96$ ($\phi = a/b = 1.25, 1.5, 2.0, 2.2, 2.5$).

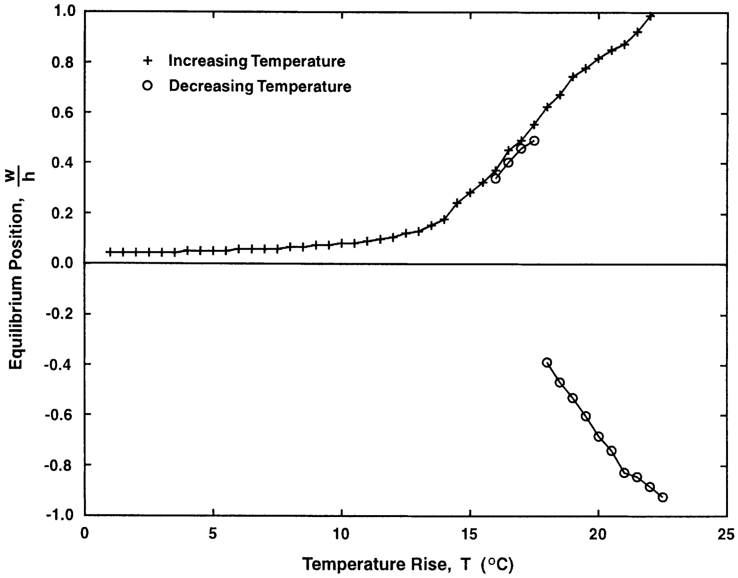

Fig. 4. An equilibrium position vs. temperature diagram for the 76.2 × 38.1 × 0.3175 cm^3 (30 × 15 × 0.125 in.) plate. The two data sets were taken by decreasing the temperature on the primary and secondary branch, respectively.

Fig. 4 shows the equilibrium position vs. temperature diagram for the $b/h = 160$ ($\phi = 1.5$) plate. Because this plate was expected to buckle in its first mode, the data was acquired near the center where the displacement was greatest, specifically at $(\xi, \eta) = (0.45, 0.45)$. The + symbols show the primary branch of the equilibrium solution. The ∘ symbols indicate the secondary branch. Clearly, as the temperature is decreased through $T = 17.25°\text{C}$, the plate passes through the saddle-node bifurcation (associated with $T_{\text{cr}}^{\text{Im}}$) and the plate snaps-through to the primary branch. As discussed previously, identifying $T_{\text{cr}}^{\text{Im}}$ is a key component to determine the actual buckling load.

A second critical step to find T_{cr}^{F} is to measure the magnitude of the imperfection *and* identify the mode into which the system buckles. This is accomplished using the LVDT to generate a displacement profile. Fig. 5 shows a series of profiles taken for the $b/h = 120$ ($\phi = 2$) plate. The first set of data was taken at $T = 17.5°\text{C}$ and is indicated by the ∘ symbols. This shows a deflection dominated by the first mode. As the temperature is increased to $T = 21.5°\text{C}$, given by the + symbols, the growing influence of the second mode is evident. The final set of data, with the × symbols, corresponds to the snapped-through position (i.e. on the secondary branch) at $T = 27.5°\text{C}$. This clearly shows the dominant second mode nature of the buckled equilibrium shape. More importantly, this figure shows the gradual evolution from a first mode initial imperfection into a second mode buckling shape.

Fig. 6 shows a similar evolution for the $b/h = 96$ ($\phi = 2.5$) plate. Here, the data sets correspond to tests at $T = 0°\text{C}$, 20°C, 35°C, and 57°C given by ∘, +, ×, ∗, respectively. At the ambient, the equilibrium shape is first mode in character. As the temperature is increased to 20°C and then to 35°C, the deflection gradually takes on three distinct humps – indicating a growing third mode contribution. At 57°C, the plate is clearly in the third mode but has been snapped through to its secondary equilibrium state.

The typical way to display the variation in the buckling parameter is to plot it against the aspect ratio. As discussed in Section 2, both the length scales a/h and b/h are relevant and simply using the aspect ratio $\phi = a/b$ is not sufficient. With this in mind, consider Fig. 7. This shows the theoretical eigenvalues (with only the first nine modes retained) for a fixed $a/h = 240$ and for decreasing b/h. This increases the aspect ratio as shown on the top scale. Note, however, that because one of the dimensions is reducing, the system

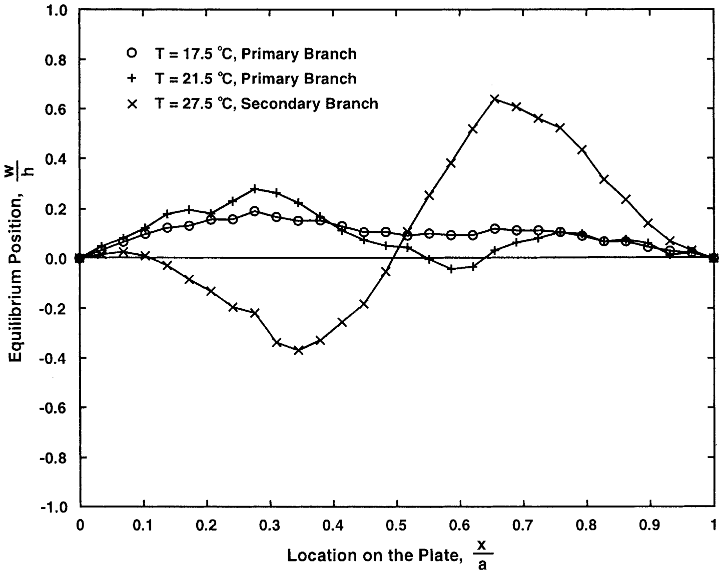

Fig. 5. Three plate profiles for the 76.2 × 30.48 × 0.3175 cm^3 (30 × 12 × 0.125 in.^{3}) plate. Data were obtained at $T = 17.5$, 21.5, 27.5°C. The (2,1) mode is clearly visible.

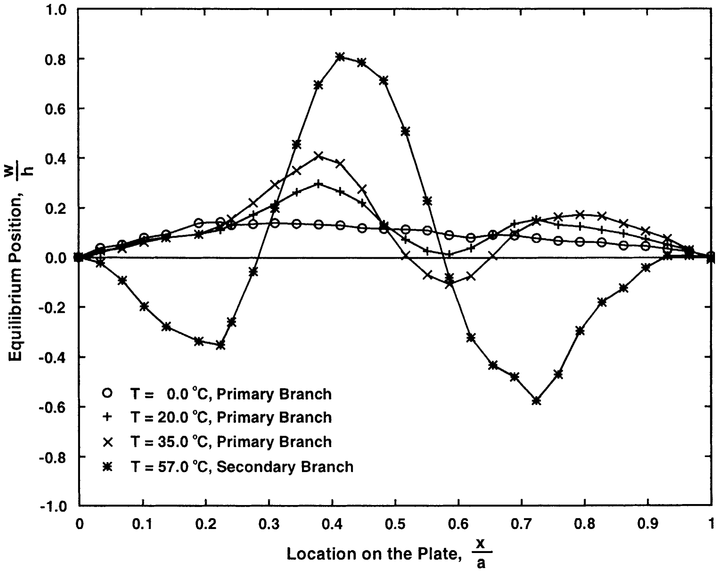

Fig. 6. Four plate profiles for the 76.2 × 30.48 × 0.3175 cm^3 (30 × 12 × 0.125 in.^{3}) plate. Data were obtained at $T = 0$, 20, 35, 57°C. The presence of the (3,1) mode is evident.

becomes stiffer. As a result, the eigenvalue loci (the lowest of which corresponds to the buckling temperature) increase rapidly. Several other features of this plot merit discussion. First, it is evident that at an aspect ratio of $\phi = 1$, the lowest eigenvalue loci relates to the (1,1) mode and the (2,1)–(1,2), (3,1)–(1,3), and (3,2)–(2,3) eigenvalues coincide. As ϕ increases, the eigenvalues fall into groups defined by their second

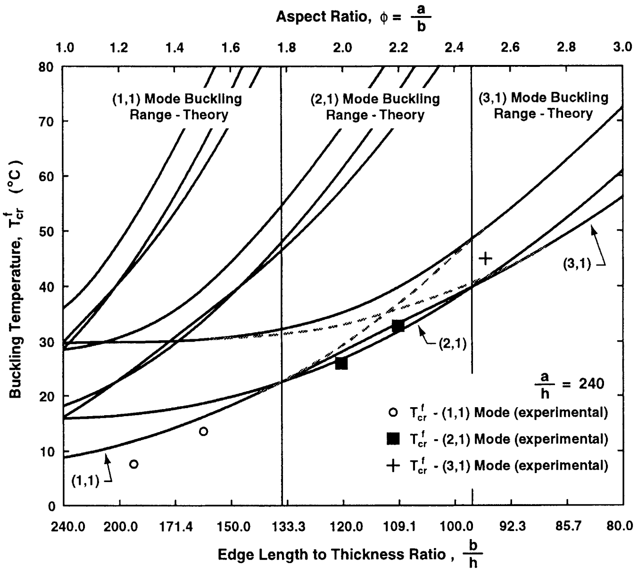

Fig. 7. The theoretical eigenvalue loci and the experimental results for increasing aspect ratios via decreasing b/h.

index – associated with the shrinking y-direction. In other words, the three groupings consist of (i) the lowest group: the (1,1), (2,1), (3,1) modes and (ii) the middle group: the (1,2), (2,2), (3,2) modes and (iii) the higher group: the (1,3), (2,3), (3,3) modes. The first grouping may be explained as follows. As the plate dimension b/h decreases, it is most likely to buckle in its first mode in the shrinking direction (given by the second index) but in sequentially higher modes in the fixed direction (given by the first index). This is also true for the other groups.

As b/h initially decreases from 240, the lowest curve is associated with the (1,1) mode. At $\phi \approx 1.785$, the (2,1) and (1,1) curves cross and the (2,1) mode becomes the buckling mode. As b/h is decreased still further, the (2,1) and (1,1) curves begin to diverge and, for a very short time, the (3,1) and (1,1) curves begin approaching one another. In this region, $1.9 < \phi < 2.4$, the (1,1) and (3,1) modes begin to mix. In other words, the eigenvectors associated with each of these two curves have a large contribution from both the (1,1) *and* the (3,1) modes. This modal coupling arises out of the fully fixed boundary conditions and occurs only between modes which are purely even or, as in this case, are purely odd. With further decreases in b/h, these two eigenvalue loci veer away from one another and do *not* cross (Plaut and Pierre, 1989 or Plaut et al., 1995). In addition, their identities are exchanged, i.e. the lower curve evolves from the (1,1) mode into the (3,1) mode. The upper curve experiences the opposite transition. This veering is made more evident by the dashed lines which represent the position of the loci had veering *not* occurred (i.e. in the absence of coupling). As a result of the veering, when the two lower curves cross again at $\phi = 2.46$, this is a crossing of the (2,1) mode with the (primarily) (3,1) mode.

Also shown in Fig. 7 are five data points. These are the buckling loads, T_{cr}^{F}, which were obtained by measuring T_{cr}^{Im} and $\tilde{A}$ and using the method developed in Section 3.3. The symbols represent measured buckling temperatures in the (1,1), (2,1), and (3,1) modes, as indicated. Fairly reasonable agreement is obvious between the actual buckling load and those predicted by the theory. Of equal importance is that the theory and experiments agree in the transition of the buckling mode with the aspect ratio. In other words, in the range $1.0 < \phi < 1.785$, the theory predicts a (1,1) mode buckling – and the experiments agree. Over the range $1.785 < \phi < 2.46$, a (2,1) mode buckling is predicted. Again, the experiments agree. For the range $2.46 < \phi$, the system is predicted to buckle in the (3,1) mode. The one data point taken in this range

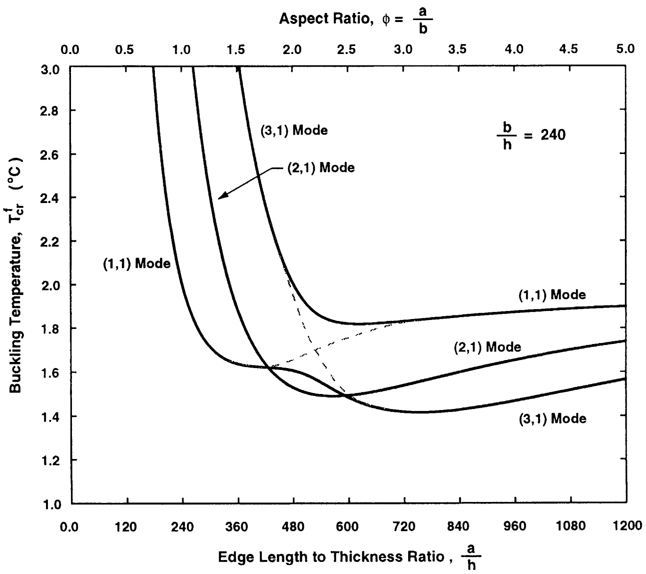

Fig. 8. The theoretical eigenvalue loci for increasing aspect ratios via increasing a/h.

(which, at $\phi = 2.5$, barely makes this neighborhood) also agrees with the theory. It should be noted that at some larger value of ϕ, the (4,1) curve would cross the (3,1) curve, making the (4,1) mode the critical mode. However, for simplicity, the theoretical calculations were limited to the first three modes in each direction for a total of nine plate modes. Hence, the (4,1) mode does not appear in these results.

Fig. 8 shows a more traditional presentation of such buckling results. In this purely theoretical set of results, b/h is held fixed at 240 and the a/h is increased, thereby increasing the aspect ratio. As a result, the actual plate size (surface area) continuously increases in contrast to the last scenario – where b/h was decreased and the area decreased. In this case, three groupings again appear but are dictated by the first index. The smallest three eigenvalue loci, constituting the lowest grouping, are shown in Fig. 8. The buckling mode transitions from the (1,1) to the (2,1) at the crossing point $\phi = 1.75$. As the a/h is increased, the eigenvalue loci experience veering between the (1,1) and the (3,1) modes. To highlight the veering, the crossing of the loci (had veering not occurred) is shown again with the dashed lines. At an aspect ratio of $\phi = 2.45$, the (2,1) and the (predominantly) (3,1) curves cross. Finally, it should be noted that the buckling temperatures are extremely low and do not increase appreciably with the aspect ratio. This is attributed to the increasing plate size. Since the plate continuously grows with ϕ, the system does not stiffen and, hence, the buckling temperature remains low.

5. Conclusions

A combined theoretical and experimental study of the buckling characteristics of thermally loaded, rectangular plates is presented. The theoretical aspect of this work involves an energy based approach to calculate the buckling temperature for plates of various sizes. It is shown that the edge length to thickness ratios, a/h and b/h, are independent parameters. Hence, the aspect ratio $\phi = a/b$, while still a physically meaningful parameter, is not sufficient to describe a problem uniquely. Results are presented which show the variation in the buckling eigenvalues as a function of one of the edge lengths (more traditionally shown as a change in the aspect ratio). The eigenvalue loci collect into groups dictated by the first (second) index of the mode number as the x-direction (y-direction) edge length is changed. In addition, curve veering, without mode localization, occurs between the purely even or purely odd modes, e.g. the (i,j)th mode veers with the (k,l)th mode provided i,j,k,l are either all odd or all even.

The experimental portion of this work also focuses on obtaining the buckling temperature as a function of the edge length. The measurements are complicated by the fact that actual plates have an inherent initial curvature. This changes the basic character of the systems equilibrium position vs. temperature diagram. Specifically, the pitchfork bifurcation associated with the perfectly flat plate disappears and is replaced by a saddle-node bifurcation at a higher temperature. As a result, measuring $T_{\mathrm{cr}}^{\mathrm{F}}$ directly is impossible. This is overcome by realizing that the separation between $T_{\mathrm{cr}}^{\mathrm{F}}$ and $T_{\mathrm{cr}}^{\mathrm{Im}}$ is a function of the imperfection size $\tilde{A}$. A functional relation is developed between these quantities of the form: $T_{\mathrm{cr}}^{\mathrm{F}}/T_{\mathrm{cr}}^{\mathrm{Im}} = f(\tilde{A})$. Using this relation with the measured values of $T_{\mathrm{cr}}^{\mathrm{Im}}$ and $\tilde{A}$ gives $T_{\mathrm{cr}}^{\mathrm{F}}$. This is done for five values of the edge to thickness ratio b/h, and comparisons with the theoretical values show good agreement for the magnitude of the buckling loads. Moreover, the experimental and theoretical results agree on the transition of the buckling modes with the edge length parameter. In other words, the predicted buckling *load* and the predicted buckling *mode* were in good agreement with the experimental results.

Acknowledgements

The support of the Structures Group at Wright–Patterson Air Force Base (grant number PO-45065) is gratefully acknowledged.

Appendix A

The single mode, algebraic equilibrium equation, Eq. (7), is obtained by satisfying the von Kármán equilibrium equation and the associated compatibility equation (Dowell, 1975). These are given by

$$\overset{\prime}{\nabla}{}^4 w - \phi^2\left[F_{,\eta\eta}(w_{,\xi\xi} + w_{0,\xi\xi}) + F_{,\xi\xi}\big(w_{,\eta\eta} + w_{0,\eta\eta}\big) - 2F_{,\xi\eta}\big(w_{,\xi\eta} + w_{0,\xi\eta}\big)\right] = 0, \tag{15}$$

$$\overset{\prime}{\nabla}{}^4 F = 12(1-\nu^2)\phi^2[(w_{,\xi\eta})^2 + 2w_{,\xi\eta}w_{0,\xi\eta} - w_{,\xi\xi}w_{,\eta\eta} - w_{,\xi\xi}w_{0,\eta\eta} - w_{,\eta\eta}w_{0,\xi\xi}], \tag{16}$$

where $w = W/h$ is the nondimensional lateral displacement of the plate, $w_0 = W_0/h$ is the initial geometric imperfection and F is the Airy stress function. The nondimensional spatial coordinates are $\xi = x/a$ and $\eta = y/b$. A nondimensional biharmonic operator is defined as $\overset{\prime}{\nabla}{}^4 = (1/a^4)[(\partial^4/\partial\xi^4) + 2(a/b)^2(\partial^4/\partial\xi^2\partial\eta^2) + (a/b)^4(\partial^4/\partial\eta^4)]$, where the comma notation refers to differentiation, i.e., $\bullet_{,\xi} = \mathrm{d}\bullet/\mathrm{d}\xi$. Finally, ν is Poisson's ratio.

Implicit in this plate theory is the fact that the initial curvatures ($w_{0,\xi\xi}$ and $w_{0,\eta\eta}$) and the squares of the slopes ($w_{0,\xi}^2$ and $w_{0,\eta}^2$) are small. Hence, they are discarded from the strain–displacement relations. This limits the applicability of this theory to small initial geometric imperfections but, fortunately, such assumptions are typically valid for small to moderate sized plates.

To arrive at Eq. (7), a solution procedure similar to that outlined by Murphy et al. (1997) is taken. The procedure is briefly reprised here for completeness. To begin, a solution to the compatibility equation is sought. A single mode displacement field of the form

$$w(\xi,\eta) = A\Psi(\xi,\eta) \quad \text{and} \quad w_0(\xi,\eta) = \tilde{A}\tilde{\Psi}(\xi,\eta) \tag{17}$$

is assumed and substituted into Eq. (16) (note that the shape functions Ψ and $\tilde{\Psi}$ need not be the same mode!). The right-hand side is grouped in terms of A^2 and $A\tilde{A}$. As a result, the particular solution takes the form $F_\mathrm{p} = A^2(\mathscr{F}^\mathrm{I}\Psi) + A\tilde{A}(\mathscr{F}^\mathrm{II}\Psi)$. The unknown coefficients $\mathscr{F}^\mathrm{I}$ and $\mathscr{F}^\mathrm{II}$ are then found by equating like terms and performing a Galerkin procedure. This process leads to

$$\mathscr{F}^\mathrm{I} = 12(1-v^2)\left(\frac{a}{b}\right)^2 \frac{\int_0^1\int_0^1 (\Psi_{,\xi\eta}^2 - \Psi_{,\xi\xi}\Psi_{,\eta\eta})\Psi\,\mathrm{d}\xi\,\mathrm{d}\eta}{\int_0^1\int_0^1 (\Psi_{,\xi\xi\xi\xi} + 2(a/b)^2\Psi_{,\xi\xi\eta\eta} + (a/b)^4\Psi_{,\eta\eta\eta\eta})\Psi\,\mathrm{d}\xi\,\mathrm{d}\eta}, \tag{18}$$

$$\mathscr{F}^\mathrm{II} = 12(1-v^2)\left(\frac{a}{b}\right)^2 \frac{\int_0^1\int_0^1 (2\Psi_{,\xi\eta}\tilde{\Psi}_{,\xi\eta} - \Psi_{,\xi\xi}\tilde{\Psi}_{,\eta\eta} - \Psi_{,\eta\eta}\tilde{\Psi}_{,\xi\xi})\Psi\,\mathrm{d}\xi\,\mathrm{d}\eta}{\int_0^1\int_0^1 (\Psi_{,\xi\xi\xi\xi} + 2(a/b)^2\Psi_{,\xi\xi\eta\eta} + (a/b)^4\Psi_{,\eta\eta\eta\eta})\Psi\,\mathrm{d}\xi\,\mathrm{d}\eta}. \tag{19}$$

The homogeneous solution to the compatibility equations may be expressed as: $F_\mathrm{h} = (N_\xi\,\eta^2 + N_\eta\,\xi^2)/2$. N_ξ and N_η may be determined by using the stress–strain relations (including thermal effects) and the strain–displacement relations. These may be expressed as

$$u_{,\xi} = \frac{1}{12(1-v^2)}\left(\frac{h}{b}\right)^2\left[F_{,\eta\eta} - v\left(\frac{b}{a}\right)^2 F_{,\xi\xi}\right] - \frac{1}{2}\left(\frac{h}{a}\right)^2 (w_{,\xi})^2 - \left(\frac{h}{a}\right)^2 w_{,\xi}w_{0,\xi} + \alpha T, \tag{20}$$

$$v_{,\eta} = \frac{1}{12(1-v^2)}\left(\frac{h}{a}\right)^2\left[F_{,\xi\xi} - v\left(\frac{a}{b}\right)^2 F_{,\eta\eta}\right] - \frac{1}{2}\left(\frac{h}{b}\right)^2 (w_{,\xi})^2 - \left(\frac{h}{a}\right)^2 w_{,\eta}w_{0,\eta} + \alpha T. \tag{21}$$

These equations may be integrated over the domain to obtain the in-plane displacements at the edges. For a plate whose edges are fully fixed in-plane, $u(0) = u(1) = v(0) = v(1) = 0$, the in-plane loads, N_ξ and N_η, are found to be

$$N_\xi = \beta_{11}A^2 + \beta_{12}A\tilde{A} + \beta_{13}\alpha T, \tag{22}$$

$$N_\eta = \beta_{21}A^2 + \beta_{22}A\tilde{A} + \beta_{23}\alpha T, \tag{23}$$

where

$$\beta_{11} = \frac{-1}{1-v^2}\int_0^1\int_0^1\left[\mathscr{F}^\mathrm{I}\Psi_{,\eta\eta}(1-v^2) - 6(1-v^2)\left(\frac{b}{a}\right)^2\left(\Psi_{,\xi}^2 + v\left(\frac{a}{b}\right)^2\Psi_{,\eta}^2\right)\right]\mathrm{d}\xi\,\mathrm{d}\eta,$$

$$\beta_{12} = \frac{-1}{1-v^2}\int_0^1\int_0^1\left[\mathscr{F}^\mathrm{II}\Psi_{,\eta\eta}(1-v^2) - 12(1-v^2)\left(\frac{b}{a}\right)^2\left(\Psi_{,\xi}\tilde{\Psi}_{,\xi} + v\left(\frac{a}{b}\right)^2\Psi_{,\eta}\tilde{\Psi}_{,\eta}\right)\right]\mathrm{d}\xi\,\mathrm{d}\eta,$$

$$\beta_{13} = \frac{-1}{1-v^2}\int_0^1\int_0^1\left[12(1-v^2)\left(\frac{b}{h}\right)^2(1+v)\right]\mathrm{d}\xi\,\mathrm{d}\eta,$$

$$\beta_{21} = \frac{-1}{1-v^2}\int_0^1\int_0^1\left[\mathscr{F}^\mathrm{I}\Psi_{,\xi\xi}(1-v^2) - 6(1-v^2)\left(\frac{a}{b}\right)^2\left(\Psi_{,\eta}^2 + v\left(\frac{b}{a}\right)^2\Psi_{,\xi}^2\right)\right]\mathrm{d}\xi\,\mathrm{d}\eta,$$

$$\beta_{22} = \frac{-1}{1-v^2}\int_0^1\int_0^1\left[\mathscr{F}^\mathrm{II}\Psi_{,\xi\xi}(1-v^2) - 12(1-v^2)\left(\frac{a}{b}\right)^2\left(\Psi_{,\eta}\tilde{\Psi}_{,\eta} + v\left(\frac{b}{a}\right)^2\Psi_{,\xi}\tilde{\Psi}_{,\xi}\right)\right]\mathrm{d}\xi\,\mathrm{d}\eta,$$

$$\beta_{23} = \frac{-1}{1-v^2}\int_0^1\int_0^1\left[12(1-v^2)\left(\frac{a}{h}\right)^2(1+v)\right]\mathrm{d}\xi\,\mathrm{d}\eta.$$

Finally, the complete Airy stress function $F = F_\mathrm{h} + F_\mathrm{p}$ and the assumed displacement field are substituted into Eq. (15) and Galerkin's procedure is applied. This produces the algebraic equilibrium equation given by Eq. (7). The Galerkin coefficients γ_i are given by

$$\gamma_1 = -\phi^2 \int_0^1 \int_0^1 [2\mathscr{F}^{\mathrm{I}} \Psi_{,\xi\xi} \Psi_{,\eta\eta} + \beta_{11} \Psi_{,\xi\xi} + \beta_{12} \Psi_{,\eta\eta} - 2\mathscr{F}^{\mathrm{I}} \Psi^2_{,\xi\eta} - 2\Psi_{,\xi\eta}(\beta_{11}\eta + \beta_{21}\xi)]\Psi \,\mathrm{d}\xi \,\mathrm{d}\eta,$$

$$\begin{aligned}\gamma_2 = -\phi^2 \int_0^1 \int_0^1 &[2\mathscr{F}^{\mathrm{I}} \Psi_{,\xi\xi} \Psi_{,\eta\eta} + \beta_{12} \Psi_{,\xi\xi} + \mathscr{F}^{\mathrm{I}}(\Psi_{,\xi\xi}\Psi_{,\eta\eta} + \Psi_{,\xi\xi}\Psi_{,\eta\eta}) + \beta_{11}\tilde{\Psi}_{,\xi\xi} + \beta_{22}\Psi_{,\eta\eta} \\ &+ \beta_{21}\tilde{\Psi}_{,\eta\eta} - 2\mathscr{F}^{\mathrm{II}}\Psi^2_{,\xi\eta} - 2\Psi_{,\xi\eta}(\beta_{12}\eta + \beta_{22}\xi) - 2\mathscr{F}^{\mathrm{I}}\Psi_{,\xi\eta}\tilde{\Psi}_{,\xi\eta} - 2\Psi_{,\xi\eta}(\beta_{11}\eta + \beta_{21}\xi)]\Psi \,\mathrm{d}\xi \,\mathrm{d}\eta,\end{aligned}$$

$$\gamma_4 = \int_0^1 \int_0^1 (\Psi_{,\xi\xi\xi\xi} + 2(a/b)^2\Psi_{,\xi\xi\eta\eta} + (a/b)^4\Psi_{,\eta\eta\eta\eta})\Psi \,\mathrm{d}\xi \,\mathrm{d}\eta,$$

$$\gamma_5 = -\phi^2 \int_0^1 \int_0^1 [\beta_{13}\Psi_{,\xi\xi} + \beta_{23}\Psi_{,\eta\eta} + 2\Psi_{,\xi\eta}(\beta_{13}\eta + \beta_{23}\xi)]\Psi \mathrm{d}\xi \,\mathrm{d}\eta,$$

$$\gamma_6 = -\phi^2 \int_0^1 \int_0^1 [\beta_{13}\tilde{\Psi}_{,\xi\xi} + \beta_{23}\tilde{\Psi}_{,\eta\eta} - 2\tilde{\Psi}_{,\xi\eta}(\beta_{13}\eta + \beta_{23}\xi)]\Psi \,\mathrm{d}\xi \,\mathrm{d}\eta.$$

Appendix B

$$C_0 = \frac{27\gamma_1^3}{\alpha^3\gamma_5^3}\left[-\left(\frac{\tilde{A}^6\gamma_2^2\gamma_3^2 + \tilde{A}^2\gamma_2^2\gamma_4^2}{108\gamma_1^4}\right) + \left(\frac{\tilde{A}^6\gamma_3^3 + \gamma_4^3}{27\gamma_1^3}\right) - \frac{\tilde{A}^4\gamma_2^2\gamma_3\gamma_4}{54\gamma_1^4} + \left(\frac{\tilde{A}^4\gamma_3^2\gamma_4 + \tilde{A}^2\gamma_3\gamma_4^2}{9\gamma_1^3}\right)\right],$$

$$\begin{aligned}C_1 = \frac{27\gamma_1^3}{\alpha^3\gamma_5^3}\Bigg[&-\left(\frac{\alpha\tilde{A}^4\gamma_2^2\gamma_3\gamma_5 + \alpha\tilde{A}^2\gamma_2^2\gamma_4\gamma_5}{54\gamma_1^4}\right) + \left(\frac{\alpha\tilde{A}^4\gamma_3^2\gamma_5 + 2\alpha\tilde{A}^2\gamma_3\gamma_4\gamma_5 + \alpha\gamma_4^2\gamma_5}{9\gamma_1^3}\right) \\ &+ \frac{\alpha\tilde{A}^4\gamma_2^3\gamma_6}{27\gamma_1^4} - \left(\frac{\alpha\tilde{A}^4\gamma_2\gamma_3\gamma_6 + \alpha\tilde{A}^2\gamma_2\gamma_4\gamma_6}{6\gamma_1^3}\right)\Bigg],\end{aligned}$$

$$C_2 = \frac{27\gamma_1^3}{\alpha^3\gamma_5^3}\left[-\frac{\alpha^2\tilde{A}^2\gamma_2^2\gamma_5^2}{108\gamma_1^4} + \left(\frac{\alpha^2\tilde{A}^2\gamma_3\gamma_5^2 + \alpha^2\gamma_4\gamma_5^2}{9\gamma_1^3}\right) - \frac{\alpha^2\tilde{A}^2\gamma_2\gamma_5\gamma_6}{6\gamma_1^3} + \frac{\alpha^2\tilde{A}^2\gamma_6^2}{4\gamma_1^2}\right].$$

References

Boley, B.A., Weiner, W., 1965. The Theory of Thermal Stresses. Wiley, New York.

Budiansky, B. (Ed.), 1976. Buckling of Structures. IUTAM Symposium, Springer, Berlin.

Dowell, E.H., 1975. Aeroelasticity of Plates and Shells. Kluwer, Netherlands.

Hoff, N.J., Boley, B.A., Coan, J.M., 1948. The development of a technique for testing stiff panels in edgewise compression. Proceedings of the Society of Experimental Stress Analysis 5, 14–24.

Meriam, L.J., Kraige, L.G., 1992. Engineering Mechanics: Dynamics, Third ed. Wiley, New York.

Murphy, K.D., Virgin, L.N., Rizzi, S.A., 1997. The effect of thermal prestress on the free vibration characteristics of thermally loaded plates: theory and experiments. Journal of Vibration and Acoustics 119, 243–249.

Plaut, R.H., Pierre, C., 1989. Curve veering and mode localization in a buckling problem. Zeitschrift Fur angewandte Mathematik und Physik 40, 758–761.

Plaut, R.H., Virgin, L.N., 1990. Use of frequency data to predict buckling. Journal of Engineering Mechanics 116 (10), 2330–2335.

Plaut, R.H., Murphy, K.D., Virgin, L.N., 1995. Curve and surface veering for a braced column. Journal of Sound and Vibration 187 (5), 879–885.

Southwell, R.V., 1932. On the analysis of experimental observations in problems of elastic stability. Proceedings of the Royal Society of London 135A, 601–616.

Souza, M.A., Fok, W.C., Walker, A.C., 1983. Review of experimental techniques for thin-walled structures liable to buckling, part 1: neutral and unstable buckling. Experimental Techniques 7 (9), 21–25.

Tauchert, T.R., 1991. Thermally induced flexure, buckling, and vibration of plates. Applied Mechanics Review 44 (8), 347–360.

Thompson, J.M.T., Hunt, G.W. (Eds.), 1983. Collapse: the buckling of structures in theory and practice. IUTAM Symposium, Cambridge University Press.

Thornton, E.A., 1993. Thermal buckling of plates and shells. Applied Mechanics Reviews 46 (10), 485–506.